Nanoscale

Cite this: *Nanoscale*, 2011, **3**, 4234

www.rsc.org/nanoscale

PAPER

Light-emitting nanocomposite CdS–polymer electrospun fibres *via in situ* nanoparticle generation

Francesca Di Benedetto,[ab] Andrea Camposeo,*[a] Luana Persano,[a] Anna Maria Laera,[c] Emanuela Piscopiello,[c] Roberto Cingolani,[d] Leander Tapfer[c] and Dario Pisignano*[ab]

Received 19th April 2011, Accepted 22nd July 2011
DOI: 10.1039/c1nr10399g

We report on the simple, *in situ* generation of CdS nanocrystals inside electrospun polymer fibres by thermal decomposition of a cadmium thiolate precursor, leading to nanocomposite light-emitting fibres. The modifications induced in the precursor by the thermal decomposition are investigated by a morphological, structural and spectroscopic analysis of the resulting nanocomposite fibres. This approach allows us to overcome nanofabrication difficulties related to disfavoured micro- or nanofluidic molecular flow as given by the direct incorporation of particles in the electrospinning solution. This method therefore enables the synthesis of luminescent, CdS-based composite fibres with emission peaked in the visible range, suitable as building blocks for nanophotonic devices based on light-emitting nanomaterials.

Introduction

Custom designed organic–inorganic hybrid materials are becoming more and more important in various research areas such as catalysis,[1] separation membranes,[2] optoelectronics,[3] and biotechnology.[4] Hybrid materials are generally composed of a polymeric matrix hosting inorganic nanoparticles, combining the complementary features of the constituents in the nanocomposite. In particular, the combination of the size-dependent properties of inorganic nanocrystals with the high surface-to-volume ratio and flexibility of polymeric micro-nanofibres has remarkable impact on both fundamental properties and technological applications.[5] Nanocomposite fibres materials can be obtained by *ex situ* or *in situ* approaches, in which inorganic nanoparticles are respectively either mechanically dispersed into an organic solution,[6] or directly generated inside a polymer matrix by chemical,[7] thermal[8] or optical[9] decomposition of precursors. The main drawback of *ex situ* methods comes from the difficulty to achieve a homogeneous dispersion of nanoparticles in the organic matrix because of usual poor miscibility, high surface free energy and strong inter-particle interactions leading to agglomeration.[6] Despite producing broader particle size distribution and surface defects, *in situ* techniques allow one to obtain better dispersion of nanoparticles, as mediated by the polymer which limits aggregation effects, confining the nucleation sites and controlling the resulting particle size and filling factors by properly engineered functional groups, matrix assembly, and cross-linking.[6,9,10]

Importantly, an often neglected, further advantage of *in situ* approaches comes from the optimisation of the flow conditions of the nanomaterials, which are critically important for realizing composite nanostructures. In fact, the incorporation of particles significantly disfavours the micro- or nanofluidic molecular flow with respect to the corresponding purely polymeric materials, because of the enhanced system viscosity and elastic, solid-like character of the composite[11] (see the following). These effects result in a much more difficult drawing of nanostructures into the composite materials by patterning or elongational methods such as nanomolding, fluidics, soft lithography, or spinning procedures, which are all based on the micro-nanoflow materials rheology. Other difficulties are related to particle aggregates clogging micro-nanochannels or needles used for pattern transfer. *In situ* methods are strategic in this respect, allowing one to fully exploit the favourable flow of organic solutions, and then proceeding to synthesise nanoparticles after complete nanostructures have been formed.

Among other methods, electrospinning (ES) is the simplest, most versatile, and effective technology for producing fibres with diameter from a few microns to tens of nanometres.[12] It relies on the reduction of the cross-section of a viscoelastic jet induced by an applied electrostatic field and by the solvent evaporation during the time of flight of a solution from a metallic needle to a collector, hence critically depending on flow conditions. Functional nanofibres are exploited as light sources,[13] in

[a]*NNL, National Nanotechnology Laboratory of CNR-Istituto Nanoscienze, Università del Salento, via Arnesano, I-73100 Lecce, Italy. E-mail: Dario.pisignano@unisalento.it; Fax: +39 0832298146; Tel: +39 0832298104; Andrea.camposeo@nano.cnr.it*
[b]*Dipartimento di Ingegneria dell'Innovazione, Università del Salento, via Arnesano, I-73100 Lecce, Italy*
[c]*ENEA, Technical Unit for Material Technologies- Brindisi Research Centre, Strada Statale 7 Appia km. 706, I-72100 Brindisi, Italy*
[d]*Istituto Italiano di Tecnologia (I.I.T.), via Morego 30, I-16163 Genova, Italy*

field-effect transistors,[14] and photovoltaics,[15] and can embed luminescent rare earth ions,[16] distributions or linear arrays of quantum dots[17] or oriented nanowires,[18] to serve as optical waveguides with subwavelength-diameter or hybrid emitters of polarised light. However, flow-favourable *in situ* processes for synthesising semiconducting nanoparticles are basically limited to gas–solid reactions on previously electrospun fibres incorporating metal salts.[5,19]

In this work, we report on the simple, *in situ* generation of CdS nanocrystals inside electrospun poly(methyl methacrylate) (PMMA) fibres by thermal decomposition of a cadmium thiolate precursor as schematised in Fig. 1. The modifications induced in the precursor are investigated by a morphological, structural and spectroscopic analysis of the composite fibres. This approach enables the synthesis of luminescent CdS-based composite fibres with emission peaked at 560–650 nm, suitable as building blocks for nanophotonic devices based on light-emitting nanomaterials.

Experimental

Precursor synthesis

The reagents used to synthesise our precursors are purchased from Aldrich, and used without further purification. Our Cd-complexes are obtained by incorporating a Lewis base (1-methylimidazole) on the cadmium-bis(benzylthiol) $[Cd(SBz)_2]_2 \cdot MI$.[20,21] Cadmium nitrate hexahydrate (9 mmol) is weighed in a flask and dissolved in ethanol. An aqueous solution of ammonium hydroxide (25%, NH_4OH) is added in order to obtain a transparent solution. By adding benzyl mercaptan ($C_6H_5CH_2SH$, 18 mmol), the desired product precipitates as a white powder. This is then filtered from the solution, washed with absolute ethanol and dried under vacuum. Finally, in order to synthesise the $Cd(SBz)_2(MI)_n$ complex, $Cd(SBz)_2$ is suspended in chloroform and 1-methylimidazole is added drop by drop until complete dissolution of thiolate.[21] The obtained product is purified through crystallization from toluene by cooling the solution at −18 °C.

The hybrid solution is prepared by firstly dissolving the precursor molecules in chloroform ($\sim 5.6 \times 10^{-2}$ M) and then gradually adding PMMA (up to $\sim 5.6 \times 10^{-2}$ M) while stirring at room temperature. After overnight stirring, 1-methylimidazole is added under N_2 atmosphere (in a ratio 1 : 10 with respect to chloroform) to improve the solubility of the precursor molecules. The final precursor/polymer solution presents a weight-ratio fixed at 25%.

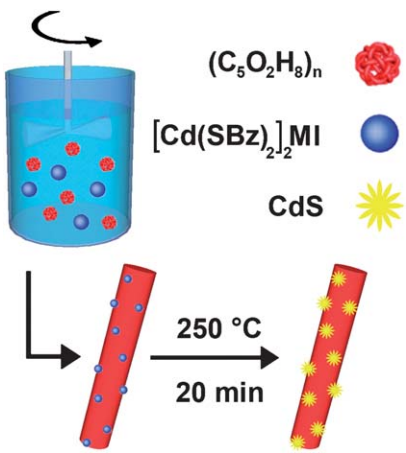

Fig. 1 Scheme of *in situ* production of CdS nanoparticles in PMMA electrospun fibres.

Realization of composite nanofibres

In a typical ES experiment, the precursor/polymer solution is placed into a plastic syringe tipped with a 19 gauge stainless steel needle. The positive lead from a high voltage supply (XRM30P, Gamma High Voltage Research) is connected to the metal needle. The solution is injected at the end of the needle at a rate in the range of 1–12 μL min^{-1} by a syringe pump (33 Dual Syringe Pump, Harvard Apparatus), in order to prevent any dripping process. The fibres are collected onto grounded targets of different substrates (quartz, Silicon and aluminium foils) placed at a distance of 12 cm from the needle. All the ES experiments are performed at room temperature with a relative air humidity of about 50%. The *in situ* synthesis of CdS nanocrystals is performed by heating the electrospun fibres at temperatures in the range of 175–250 °C for 20 minutes. The thermal treatment is performed under N_2 atmosphere (pressure = 2.6 bar, water and oxygen contents below 31.8 ppm) to avoid possible damage of the fibre constituents induced by oxygen.

SEM, TEM and XRD characterization

The scanning electron microscopy (SEM) investigation is carried out by a Raith 150 electron beam system operating with an acceleration voltage of 5–20 kV and an aperture of 20–60 μm. Low-resolution transmission electron microscopy (TEM) pictures are obtained using a Jeol Jem 1011 microscope operating at 100 kV, preparing samples by direct ES on a TEM carbon-coated copper grid (TAAB, Laboratories Equipment Ltd), and then heated at 250 °C for 20 minutes under N_2 to synthesise CdS nanocrystals. High-resolution measurements are performed by a TECNAI F30 transmission electron microscope operating at 300 kV and a point-to-point resolution of ≅0.2 nm. Cross-sectional TEM specimens are prepared by ultramicrotomy, after depositing a 200-nm gold film on fibres to have a high-contrast material on top of the low-contrast organic material. Samples, consisting of a thin Al foil, the composite fibres, and the Au layer, are cut into small slices and embedded in epoxy resin, and ultra-thin sections (~90 nm in thickness) are cut at room temperature with a diamond knife using the ultramicrotome TOP ULTRA 170A (W. Pabisch). The slices are floated on distilled water and transferred to TEM specimen support grids. X-Ray diffraction measurements are carried out under glancing incidence conditions by a diffractometer in a parallel beam geometry (Philips MPD PW1880, 3 kW generator). For all the measurements, CuKα-radiation ($\lambda_{CuK\alpha} = 0.154186$ nm) is used. Glancing incidence X-ray diffraction (GIXRD) patterns are recorded by maintaining the incident angle ω_i (angle between the incident beam and sample surface) fixed at 1.0° and moving the X-ray detector and post-sample flat graphite collimator–monochromator along the goniometer circle in the 2θ range between 10° and 80° with a step size of 0.02°.

Rheological and optical characterization

Rheological measurements are carried out by a rotational rheometer (TA Instruments Inc., New Castle, DE). Samples of precursor-doped PMMA, before and after thermal treatment at 250 °C, are prepared as disks of about 1 mm thickness and 25 mm diameter, and studied using the parallel plate geometry, at 170 °C under nitrogen atmosphere.

Fourier transform infrared spectra are measured with a spectral resolution of 4 cm^{-1} by a Spectrum 100 spectrometer (Perkin Elmer) equipped with an attenuated total reflectance accessory, with a mounted Zn–Se crystal for coupling. For these measurements, 2 × 3 cm^2 fibre samples are prepared by continuous ES runs over 6 h, using an Al foil as collector. Fluorescence images are collected by an inverted fluorescence microscope (Olympus IX71), equipped with a high-pressure Hg lamp and fitted with a digital camera (Leica). Photoluminescence (PL) measurements are performed by exciting samples with a He–Cd laser ($\lambda = 325$ nm, excitation fluence < 0.1 W cm^{-2}) and collecting the forward emission signal using a fibre-coupled monochromator (iHR320, Jobin Yvon) equipped with a charge coupled device (Simphony, Jobin Yvon). All the optical characterizations are performed at room temperature in air.

Results and discussion

The adducts used here are easy to prepare, stable under normal conditions and allow to reach moderately high concentration (up to 25%) without aggregation effects. After PMMA, 1-methylimidazole is also added to the hybrid solution in order to improve the solubility of the precursor molecules. The excellent processability of PMMA allows to directly electrospin the optically transparent and homogeneous solution, thus collecting nonwoven mats of dry fibres. In this framework, the polymer phase acts both as stabilizing and confining agent for the growth of nanoparticles and as suitable host able to overcome the poor viscoelastic behaviour of the low molar-mass precursor molecule. The resulting fibres, imaged by SEM, exhibit a smooth and featureless surface and quite uniform diameter (Fig. 2a). For instance, the diameter distribution of fibres realized with an ES injection rate (Q) of 12 μL min^{-1} and a bias of 6 kV peaks at 330 nm (Fig. 2b), whereas thinner fibres (down to 240 nm) are produced when Q is decreased to 1 μL min^{-1} (inset in Fig. 2b). Upon collection, fibres undergo a thermal treatment at temperatures in the range of 175–250 °C for 20 minutes, which decomposes the precursor to obtain nanosized CdS crystals in the PMMA fibres (see the following). Afterwards, first evidence of the formation of CdS nanoparticles comes from the colour change of the fibres from white opalescent to yellow. No significant variation is measured on the average fibre diameter, notwithstanding a slight increase of the surface roughness because of the generation of entrapped CdS nanocrystals.

Firstly, the enhancement of the system viscosity (η) as a consequence of nanoparticle formation upon thermal annealing is observed in our system by rotational viscosimetry for frequency (ω) values between 10^{-3} and 80 s^{-1} (Fig. 3). With respect to pristine samples, η increases by about two to seven times after annealing (depending on the shear-rate), consistent with the growth of nanocrystals in the nanocomposite, which

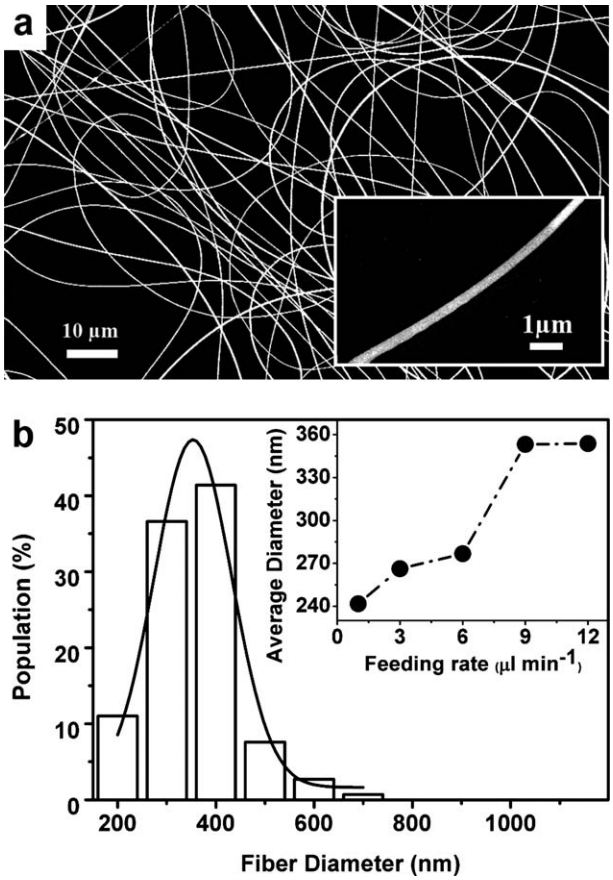

Fig. 2 (a) SEM micrographs of precursor-containing PMMA fibres. Inset: magnified view of a single fibre. (b) Typical diameter distribution. Needle–collector distance = 12 cm. The superimposed line is the best fit by a Gaussian curve (full width at half maximum ≅ 180 nm). Inset: average diameters of fibres *vs.* ES injection rate. Needle–collector distance = 12 cm. Applied bias = 6 kV.

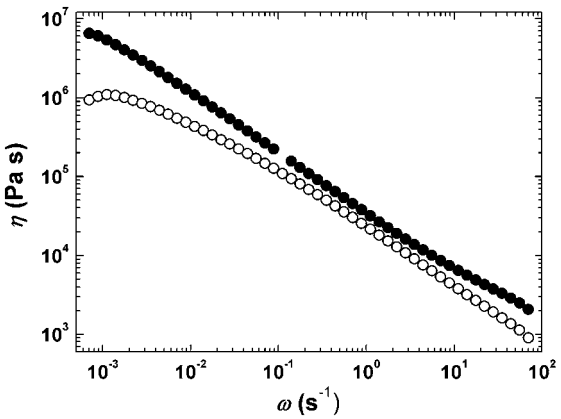

Fig. 3 Frequency dependence of viscosity, η, of precursor-doped PMMA, before (empty circles) and after (full circles) thermal treatment at 250 °C.

provides resistance to melt flow and deformations. In particular, this finding confirms that electrospinning of the nanocomposite after the *in situ* synthesis of nanoparticles would be harder or

even prevented by the higher material viscosity. Furthermore, a shear-thinning behaviour is appreciable in all the investigated ranges of ω (Fig. 3), and particularly for the composite system.

The interaction between the polymer phase and the dispersed nano-sized component is studied by comparing the infrared absorption frequency of composite fibres with respect to that of PMMA. The bare PMMA spectrum (Fig. 4a) shows an intense peak at 1723 cm^{-1}, which can be attributed to stretching vibrations of ester carbonyl group C=O, together with a broad band ranging from 1270 to 1000 cm^{-1} due to C–O stretching modes and a band from 950 to 650 cm^{-1} due to C–H bending modes.[22] A new set of bands come out in the spectrum due to the presence of $[Cd(SBz)_2]_2 \cdot MI$, including peaks around 1530 cm^{-1}, attributed to the 1-methylimidazole molecules[23] and peaks centred at around 1600 and 700 cm^{-1} attributed to the cadmium-bis(benzylthiol) molecules.[20] These peaks disappear after the thermal treatment because of the decomposition of the precursor molecule, whereas the PMMA peaks are still present without significant variation of their relative intensities, which suggest the absence of chemical bonding or strong interaction between the polymeric matrix and the nanocrystals (Fig. 4b). The peaks assigned to the 1-methylimidazole molecule are also observed after the thermal treatment, evidencing that most of this by-product is trapped into the polymer matrix. In fact, thermal analysis evidences that they do not play a role in the *in situ* synthesis process of the CdS nanocrystals, since they favour only the thermal decomposition of the $[Cd(SBz)_2]_2 \cdot MI$ molecules.[20,21]

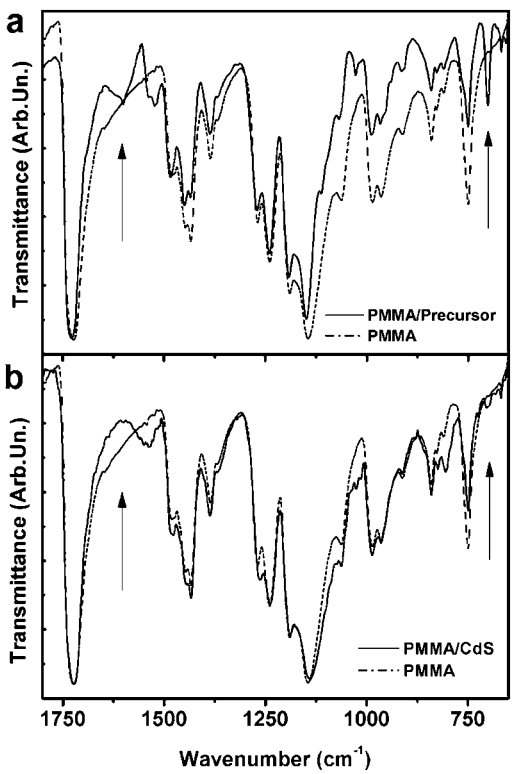

Fig. 4 FT-IR absorption spectra of nanocomposite fibres before (a) and after (b) thermolysis process of the embedding precursor (continuous line) with respect to pure PMMA (dashed line) nanofibre non-woven mats. The arrows highlight modes attributed to the precursor.

As shown in the inset of Fig. 5, X-ray scattering measurements on the as-deposited system (PMMA polymer doped with the precursor molecules) exhibit characteristic X-ray peaks that are related to the spatial ordering of the precursor molecules within the PMMA polymer.[21] Here, the diffuse scattering peaks of the PMMA polymer and the background scattering are subtracted in order to analyze the characteristic X-ray peaks of the precursor. Analogous to findings from FT-IR analysis, we find that the subsequent heat treatment causes a decomposition of the precursor molecules leading to the loss of their spatial ordering and, consequently, reducing the X-ray intensity of the Bragg peaks. To monitor the process, two Bragg peaks located at $2\theta = 25.5°$ and $2\theta = 30.9°$, respectively, are selected, allowing to probe the X-ray intensity as a function of the heat treatment temperature. The X-ray peak intensity is reduced by about 50% at an annealing temperature of 175 °C, whereas no Bragg peaks can be observed for temperatures above 220 °C (Fig. 5). This finding clearly indicates that after annealing at 220 °C, there is no spatial arrangement and ordering of the precursor molecules. The loss of spatial ordering of the precursor within the polymer matrix is related to the molecular decomposition.

This conclusion is also supported by thermogravimetric measurements, performed on the precursor system without embedding the polymer in order to investigate the thermal decomposition avoiding any possible influence of the matrix material. As previously mentioned, the TGA measurements show that at a temperature of 160 °C, the weight loss is about 9.1% and can be ascribed to the CH_3–imidazole ligand cleavage.[20] At higher temperature (244 °C), which corresponds to the maximum heat absorption, the mass reduction is of almost 55%, which is in good agreement with the calculated weight percentage of 59.7% of the dibenzyl sulfide.[20] This organic subproduct is probably fragmented in higher volatile compounds removed as gas from the platinum crucible of the thermal analyzer. Overall, the decomposition of the precursor can be summarized in a two-step process:

$$[Cd(SCH_2C_6H_5)_2]_2 \cdot MI \rightarrow 2Cd(SCH_2C_6H_5)_2 + MI \rightarrow 2CdS + 2C_6H_5CH_2SCH_2C_6H_5$$

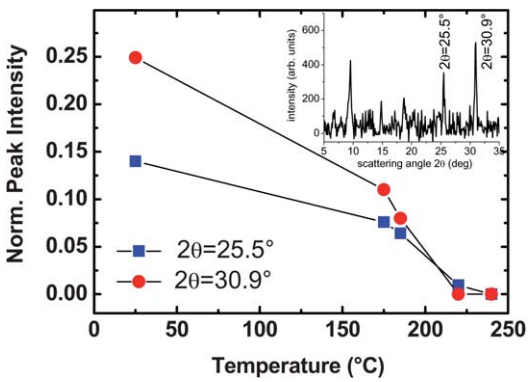

Fig. 5 Variation of the X-ray intensity of the characteristic Bragg peaks of the $[Cd(SBz)_2]_2 \cdot MI$ precursor as a function of the thermal treatment temperature. The inset shows the as measured X-ray scattering pattern prior to the thermal treatment and the two Bragg peaks located at $2\theta = 25.5°$ and 30.9°, respectively, chosen for monitoring the precursor decomposition.

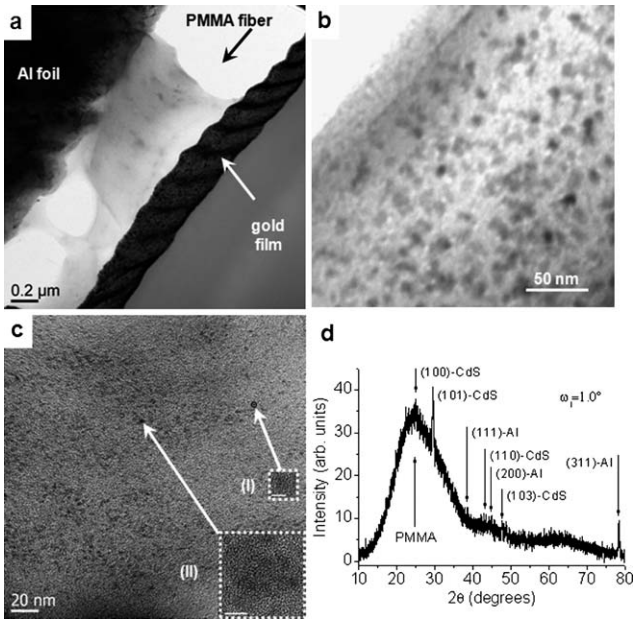

Fig. 6 Structural characterization of the nanocomposite fibres. (a) Low-magnification cross-section TEM of an individual PMMA fibre sandwiched between an Al foil and a deposited Au film. Fibre diameter ≅ 400 nm. The plait-shaped or ring-shaped morphology of the gold film is due to diamond knife of ultramicrotome cutting during TEM specimen preparation. (b) TEM micrograph of CdS nanoparticles formed in PMMA fibres. Scale bar = 200 nm. (c) Bright-field TEM image evidencing the particle distribution (the nanocrystals have darker contrast on a bright background). Inset: magnification of 3 nm (I, scale bar = 3 nm) and 15 nm (II, scale bar = 5 nm) particles. In both cases, lattice fringes are well visible. (d) GIXRD pattern of nanocomposite fibres.

One concludes therefore that the precursor molecules are completely decomposed at a temperature of 250 °C used for the fibre thermal treatment.

Indeed, TEM on fibres that have undergone thermal annealing reveals particles, roughly spherical in shape and homogeneously dispersed within the host polymer matrix, with a weak tendency to aggregate indicating that the precursor solution is stable during the ES process (Fig. 6a and b). At high magnification, CdS nanoparticles are distinguishable in the matrix (Fig. 6c), with a roughly bimodal size distribution including populations with a diameter of about 3 nm and of 10–15 nm (insets I and II of Fig. 6c, respectively). In both cases, the CdS nanocrystals display the wurzitic structure, as confirmed by high-resolution TEM images showing well-defined lattice fringes (insets of Fig. 6c).

These results are also confirmed by GIXRD measurements. A GIXRD pattern, recorded with an incidence angle, $\omega_i = 1.0°$, is displayed in Fig. 6d. In this experimental configuration, the X-ray penetration depth is reduced, enhancing the sensitivity of the measurement. The pattern exhibits a broad peak at about $2\theta = 24°$ due to the PMMA polymer, and Bragg diffraction peaks that can be attributed to the wurtzite phase of CdS (ICDD, no. 80-0006) [The International Centre for Diffraction Data, JCPDS © 2000] and the cubic Al (ICDD, no. 85-1327) of the used substrate foil. The CdS nanocrystal size, estimated from the full width at half maximum of the most intense (101)-CdS Bragg peak by using Scherrer's formula, is of about 12 nm, which is in good agreement with the TEM results.[24]

Finally, the optical properties of the nanocomposite fibres are evaluated by fluorescence microscopy and photoluminescence (PL) analysis. The fluorescence micrograph of the CdS/PMMA fibre after the thermolysis process is shown in Fig. 7a, highlighting a uniform and homogeneous bright emission which confirms the homogeneous dispersion of particles within the fibres. The room temperature PL spectra of the hybrid fibres before and after the thermal treatment, performed at different temperatures in the range 175–250 °C, are compared in Fig. 7b. Upon nucleation of CdS nanocrystals inside the fibres, an intense emission peak emerges in the visible range, red-shifting from 560 nm to 650 nm upon increasing the temperature of the thermal treatment. The absence of a significant emission signal before the thermal treatment rules out ES-induced decompositions of the precursor molecules.

The PL emission typically observed in CdS nanocrystals can be attributed to a superposition of different contributions. In bulk CdS, the band-edge emission is peaked around 515 nm at room temperature,[25] whereas a shift to higher energies of the band-edge emission is observed upon reducing the nanocrystal diameter below 9 nm.[26] In addition, the nanocrystal high surface-area-to-volume

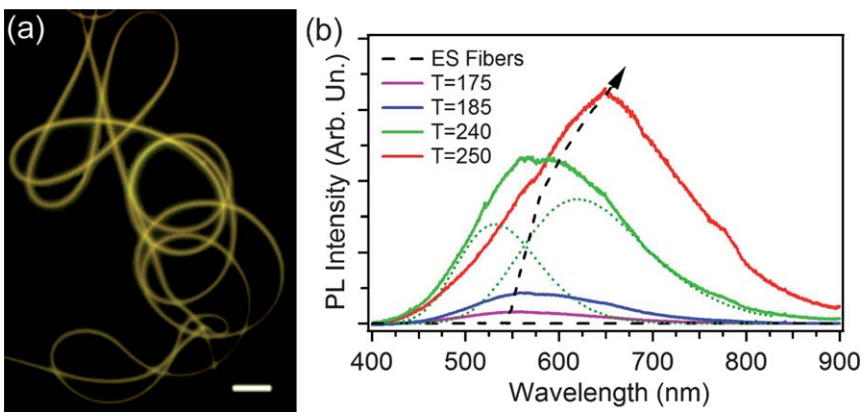

Fig. 7 (a) Fluorescence micrograph of the nanocomposite fibres. Scale bar = 20 μm. (b) Fibre PL spectra, before (dashed lines) and after (solid lines) thermal treatment, performed at 175, 185, 240, and 250 °C, respectively. The dashed arrow evidences the red shift of the overall emission peak. The dotted lines evidence the band-edge and trap state emission bands obtained by deconvolution by Gaussian functions of the emission spectrum of the sample treated at 240 °C.

ratio is often responsible for emission from surface trap states, displaying spectral features depending on the synthesis method, the storage conditions and the exposure to air or oxygen. Typically, emission from defects occurs at around 540 nm for shallow defects and at about 620 nm for deep trap states.[9,27] The emission spectrum of the nanocomposite fibres measured here is therefore ascribed to the convolution of both band-edge and defect emission (see for instance the dotted curves deconvolving the spectrum of the sample treated at 240 °C in Fig. 7), with a dominant component from the latter levels. The relative increase of the defect emission intensity by increasing the thermal treatment temperature produces the red-shift of the observed PL spectra. We point out that such features are commonly observed for *in situ* synthesised nanoparticles, because of the lack of surface passivation.[6]

Conclusions

In conclusion, we realize nanocomposite electrospun fibres embedding CdS nanocrystals with wurtzitic structure, through an *in situ* thermolytical decomposition of precursor molecules. The strategy shown here opens new possibilities for the realization of composite organic–inorganic fibres with tunable emission, overcoming flow problems inherently related to ES of particle solutions. Applied to functional polymers, this approach will be useful to produce composite nanofibres with improved optoelectronic properties, suitable for nanoscale light-source and/or photon detection.

Acknowledgements

The authors acknowledge R. Stabile and A. Polini for SEM and TEM images, S. Molle for rheological measurements, E. Pesce for cross-sectional TEM sample preparation, M. Schioppa for thermogravimetric analysis, and M. Polo for the PL measurements, respectively. Financial support by the Apulia Regional Strategic project PS_016 ("PONAMAT") and by the FIRB Project RBFR08DJZI "Futuro in Ricerca" is also gratefully acknowledged.

Notes and references

1 M. Ooe, M. Murata, T. Mizugaki, K. Ebitani and K. Kaneda, *Nano Lett.*, 2002, **2**, 999; Y. H. Zhu, L. P. Stubbs, F. Ho, R. Z. Liu, C. P. Ship, J. A. Maguire and N. S. Hosmane, *ChemCatChem*, 2010, **2**, 365.
2 T. C. Merkel, B. D. Freeman, R. J. Spontak, Z. He, I. Pinnau, P. Meakin and A. J. Hill, *Science*, 2002, **296**, 519; A. Yamaguchi, F. Uejo, T. Yoda, T. Uchida, Y. Tanamura, T. Yamashita and N. Teramae, *Nat. Mater.*, 2004, **3**, 337.
3 N. Tessler, V. Medvedev, M. Kazes, S. Kan and U. Banin, *Science*, 2002, **295**, 1506; C. Sanchez, B. Lebeau, F. Chaput and J. P. Boilot, *Adv. Mater.*, 2003, **15**, 1969; S. A. McDonald, G. Konstantatos, S. Zhang, P. W. Cyr, E. J. D. Klem, L. Levina and E. H. Sargent, *Nat. Mater.*, 2005, **4**, 138; T. Rauch, M. Böberl, S. F. Tedde, J. Fürst, M. V. Kovalenko, G. N. Hesser, U. Lemmer, W. Heiss and O. Hayden, *Nat. Photonics*, 2009, **3**, 332.
4 B. Y. S. Kim, W. Jiang, J. Oreopoulos, C. M. Yip, J. T. Rutka and W. C. W. Chan, *Nano Lett.*, 2008, **8**, 3887; Q. Zhang, T. Atay, J. R. Tischler, M. S. Bradley, V. Bulović and A. V. Nurmikko, *Nat. Nanotechnol.*, 2007, **2**, 555; E. Ruiz-Hitzky, M. Darder, P. Aranda and K. Ariga, *Adv. Mater.*, 2010, **22**, 323; V. Biju, T. Itoh and M. Ishikawa, *Chem. Soc. Rev.*, 2010, **39**, 3031.
5 X. Lu, C. Wang and Y. Wei, *Small*, 2009, **5**, 2349.
6 A. A. R. Neves, A. Camposeo, R. Cingolani and D. Pisignano, *Adv. Funct. Mater.*, 2008, **18**, 751; N. Tomczak, D. Jańczewski, M. Han and G. J. Vancso, *Prog. Polym. Sci.*, 2009, **34**, 393; H. Zhang, J. Han and B. Yang, *Adv. Funct. Mater.*, 2010, **20**, 1533.
7 S. H. Yu, M. Yoshimura, J. M. C. Moreno, T. Fujiwara, T. Fujino and R. Teranishi, *Langmuir*, 2001, **17**, 1700; H. Du, G. Q. Xu, W. S. Chin, L. Huang and W. Ji, *Chem. Mater.*, 2002, **14**, 4473; T. Cui, F. Cui, J. Zhang, J. Wang, J. Huang, C. Lu, Z. Chen and B. Yang, *J. Am. Chem. Soc.*, 2006, **128**, 6298.
8 T. Di Luccio, A. M. Laera, L. Tapfer, S. Kempter, R. Kraus and B. Nickel, *J. Phys. Chem. B*, 2006, **110**, 12603; A. C. Patel, S. Li, C. Wang, W. Zhang and Y. Wei, *Chem. Mater.*, 2007, **19**, 1231; H. C. Leventis, S. P. King, A. Sudlow, M. S. Hill, K. C. Molloy and S. A. Haque, *Nano Lett.*, 2010, **10**, 1253.
9 A. Athanassiou, R. Cingolani, E. Tsiranidou, C. Fotakis, A. M. Laera, E. Piscopiello and L. Tapfer, *Appl. Phys. Lett.*, 2007, **91**, 153108.
10 Z. B. Sun, X. Z. Dong, W. Q. Chen, S. Nakanishi, X. M. Duan and S. Kawata, *Adv. Mater.*, 2008, **20**, 914.
11 L. Persano, S. Molle, S. Girardo, A. A. R. Neves, A. Camposeo, R. Stabile, R. Cingolani and D. Pisignano, *Adv. Funct. Mater.*, 2010, **20**, 1533.
12 D. Li and Y. N. Xia, *Adv. Mater.*, 2004, **16**, 1151; A. Greiner and J. H. Wendorff, *Angew. Chem., Int. Ed.*, 2007, **46**, 5670.
13 J. M. Moran-Mirabal, J. D. Slinker, J. A. DeFranco, S. S. Verbridge, R. Ilic, S. Flores-Torres, H. Abruña, G. G. Malliaras and H. G. Craighead, *Nano Lett.*, 2007, **7**, 458; A. Camposeo, F. Di Benedetto, R. Stabile, R. Cingolani and D. Pisignano, *Appl. Phys. Lett.*, 2007, **90**, 143115; F. Di Benedetto, E. Mele, A. Camposeo, A. Athanassiou, R. Cingolani and D. Pisignano, *Adv. Mater.*, 2008, **20**, 314; F. Di Benedetto, A. Camposeo, S. Pagliara, E. Mele, L. Persano, R. Stabile, R. Cingolani and D. Pisignano, *Nat. Nanotechnol.*, 2008, **3**, 614; A. Camposeo, F. Di Benedetto, R. Stabile, A. A. R. Neves, R. Cingolani and D. Pisignano, *Small*, 2009, **5**, 562; S. Pagliara, A. Camposeo, A. Polini, R. Cingolani and D. Pisignano, *Lab Chip*, 2009, **9**, 2851.
14 A. Babel, D. Li, Y. Xia and S. A. Jenekhe, *Macromolecules*, 2005, **38**, 4705; H. Liu, C. H. Reccius and H. G. Craighead, *Appl. Phys. Lett.*, 2005, **87**, 253106; D. Tu, S. Pagliara, A. Camposeo, L. Persano, R. Cingolani and D. Pisignano, *Nanoscale*, 2010, **2**, 2217.
15 H. S. Shim, S. I. Na, S. H. Nam, H. J. Ahn, H. J. Kim, D. Y. Kim and W. B. Kim, *Appl. Phys. Lett.*, 2008, **92**, 183107; R. Zhu, C. Y. Jiang, X. Z. Liu, B. Liu, A. Kumar and S. Ramakrishna, *Appl. Phys. Lett.*, 2008, **93**, 013102.
16 G. Dong, X. Xiao, Y. Chi, B. Qian, X. Liu, Z. Ma, S. Ye, E. Wu, H. Zeng, D. Chen and J. Qiu, *J. Phys. Chem. C*, 2009, **113**, 9595; G. Dong, X. Xiao, Y. Chi, B. Qian, X. Liu, Z. Ma, E. Wu, H. Zeng, D. Chen and J. Qiu, *J. Mater. Chem.*, 2010, **20**, 1587.
17 S. Schlecht, S. Tan, M. Yosef, R. Dersch, J. H. Wendorff, Z. Jia and A. Schaper, *Chem. Mater.*, 2005, **17**, 809; H. Q. Liu, J. B. Edel, L. M. Bellan and H. G. Craighead, *Small*, 2006, **2**, 495.
18 M. Bashouti, W. Salalha, M. Brumer, E. Zussman and E. Lifshitz, *ChemPhysChem*, 2006, **7**, 102.
19 X. Lu, Y. Zhao and C. Wang, *Adv. Mater.*, 2005, **17**, 2485.
20 W. S. Rees and G. Kräuter, *J. Mater. Res.*, 1996, **11**, 3005.
21 V. Resta, A. M. Laera, E. Piscopiello, M. Schioppa and L. Tapfer, *J. Phys. Chem. C*, 2010, **114**, 17311.
22 I. K. Kang, B. K. Kwon, J. H. Lee and H. B. Lee, *Biomaterials*, 1993, **14**, 787; M. Sivakumar and K. P. Rao, *React. Funct. Polym.*, 2000, **46**, 29.
23 J. Sadlej, A. Jaworski and K. Miaskiewicz, *J. Mol. Struct.*, 1992, **274**, 247; A. Chowdhury and S. T. Thynell, *Thermochim. Acta*, 2006, **443**, 159.
24 We point out that XRD is much more sensitive to larger crystallite sizes because the broad polymer peak hides the weaker and broader contributions of the Bragg peaks of small nanocrystals.
25 H. Tong and Y. J. Zhu, *Nanotechnology*, 2006, **17**, 845; N. Pinna, K. Weiss, J. Urban and M. P. Pileni, *Adv. Mater.*, 2001, **13**, 261.
26 T. Vossmeyer, L. Katsikas, M. Giersig, G. I. Popovic, K. Diesner, A. Chemseddine, A. Eychmüller and H. Weller, *J. Phys. Chem.*, 1994, **98**, 7665; B. Yang, J. E. Schneeloch, Z. Pan, M. Furis and M. Achermann, *Phys. Rev. B: Condens. Matter Mater. Phys.*, 2010, **81**, 073401.
27 K. K. Nanda and S. N. Sahu, *Solid State Commun.*, 1999, **111**, 671; C.-W. Wang and M. G. Moffit, *Langmuir*, 2004, **20**, 11784; R. Premachandran, S. Banerjee, V. T. John, G. L. McPherson, J. A. Akkara and D. L. Kaplan, *Chem. Mater.*, 1997, **9**, 1342–1347.